Soft Matter

Accepted Manuscript

This is an *Accepted Manuscript*, which has been through the Royal Society of Chemistry peer review process and has been accepted for publication.

Accepted Manuscripts are published online shortly after acceptance, before technical editing, formatting and proof reading. Using this free service, authors can make their results available to the community, in citable form, before we publish the edited article. We will replace this *Accepted Manuscript* with the edited and formatted *Advance Article* as soon as it is available.

You can find more information about *Accepted Manuscripts* in the Information for Authors.

Please note that technical editing may introduce minor changes to the text and/or graphics, which may alter content. The journal's standard Terms & Conditions and the Ethical guidelines still apply. In no event shall the Royal Society of Chemistry be held responsible for any errors or omissions in this *Accepted Manuscript* or any consequences arising from the use of any information it contains.

ROYAL SOCIETY OF CHEMISTRY

www.rsc.org/softmatter

CREATED USING THE RSC LaTeX PCCP ARTICLE TEMPLATE – SEE www.rsc.org/electronicfiles FOR DETAILS

Modelling the Superspreading of Surfactant-laden Droplets with Computer Simulation

Panagiotis E. Theodorakis,[a] Erich A. Müller, [a] Richard V. Craster,[b] and Omar K. Matar[a]

Received Xth XXXXXXXXXX 20XX, Accepted Xth XXXXXXXXX 20XX
First published on the web Xth XXXXXXXXXX 200X
DOI: 10.1039/b000000x

The surfactant-driven superspreading of droplets on hydrophobic substrates is considered. A key element of the superspreading mechanism is the adsorption of surfactant molecules from the liquid–vapour interface onto the substrate through the contact line, which must be coordinated with the replenishment of interfaces with surfactant from the interior of the droplet. We use molecular dynamics simulations with coarse-grained force fields to provide a detailed structural description of the droplet shape and surfactant dynamics during the superspreading process. We also provide a simple method for accurate estimation of the contact angle subtended by the droplets at the contact line.

1 Introduction

Controlling the wetting of solid substrates by aqueous droplets, which is central to numerous industrial and daily-life applications, requires a fundamental understanding of spreading phenomena;[1–3] these applications include coating technology, enhanced oil recovery, drug and herbicides delivery[4] which involve the spreading of aqueous drops on hydrophobic substrates via the use of surfactants[5]. Although aqueous solutions containing surfactants are commonly used in many applications, a comprehensive understanding of the microscopic role of surfactant molecules in spreading phenomena remains challenging.[2–4,6] While experimental and theoretical studies have discussed possible mechanisms of spreading for surfactant-laden droplets,[2–4] molecular-scale simulations are indispensable for capturing the microscopic behaviour of surfactants associated with those mechanisms. To this end, molecular-level simulations[7] based on a coarse-grained force-field have recently unveiled the mechanism of superspreading,[6,8–11] which enables certain surfactants[12] to drive the anomalously fast[13] and complete wetting of moderately hydrophobic substrates.[9]

Previous work had initially focused on the study of aqueous and polymeric droplets on various technologically relevant substrates by using all-atom[14–17] and coarse-grained models.[18–34] The progress in computational capacity and the availability of reliable force-fields has further enabled the faithful modelling of surfactants in bulk aqueous solutions[35–41] suggesting links between the behaviour of surfactants in the bulk and their role in spreading processes.[42–45] In this context, the superspreading mechanism[12] and the main characteristics of superspreading surfactants have attracted much interest over the last years.[7,42–46] In spite of this, fundamental understanding of many aspects of superspreading remains lacking.

Our aim in this article is to perform large-scale molecular dynamics (MD) simulations, using coarse-grained force fields, to gain this fundamental understanding with key issues being to: identify the different stages of the superspreading process, the dependence of the final contact area on surfactant concentration, and the distribution of surfactant and water molecules in the bulk and at the vapour-liquid and liquid-solid interfaces; we will also include a reliable method to estimate the macroscopic contact angle of aqueous droplets required for the parametrization of fluid–substrate interactions in a coarse-grained model.

2 Model and methods

2.1 Molecular dynamics simulations

Here, we use MD simulations of a coarse-grained model to study aqueous droplets. Henceforth, the Boltzmann constant is taken as unity and m and σ are the reduced units for the mass and the size of the beads, respectively, while ε defines the energy scale. Hence, the time unit is $\tau = \sigma(m/\varepsilon)^{1/2}$.

All simulations are realised in the NVT ensemble by using the Nosé-Hoover thermostat as implemented in the HOOMD package[47], with an integration time-step of $\Delta t = 0.005\tau$, on GPGPUs. In addition, we have implemented the wall potential that describes the interactions between the fluid phase and the substrate[48] (Eq. 4). The number of particles and the volume of the simulation box are kept constant during the simulations,

---

[a] *Department of Chemical Engineering, Imperial College London, South Kensington Campus, London SW7 2AZ, United Kingdom*
[b] *Department of Mathematics, Imperial College London, South Kensington Campus, London SW7 2AZ, United Kingdom*

Soft Matter Accepted Manuscript

while temperature fluctuates around a predefined value, $T = 0.6057$ (corresponding to $25°C$).

For surfactant-free aqueous droplets, the total number of water beads (N) in the simulation box varies from 2×10^3 to 24×10^4 beads. For surfactant-laden aqueous droplets, the total number of beads in the simulation box is 8×10^4. The lengths of our trajectories for the surfactant-laden droplets depend on the time required for the droplets to reach an equilibrium state. In this case, typical trajectory lengths are between 10^7 and 10^8 MD time-steps depending on surfactant concentration. For surfactant-free aqueous droplets, the trajectories were 2×10^6 MD time-steps after equilibration runs of up to 10^6 MD time-steps depending on the size of the droplet (cf. Fig. 1b, c). Trajectory samples were collected every 10^4 MD time-steps for all cases, which guarantees the collection of independent statistical samples required for the analysis of the trajectories.

The simulation box for the spherical cap droplets, rectangular in shape, is 201σ long in the x and y directions, which guarantees that periodic images even of the largest droplet do not interact with each other due to the presence of periodic boundary conditions in these directions. In the z direction, beads were constrained by two walls normal to the z direction and parallel in the x and y directions. The distance between these two walls was typically 90σ for the droplets of the spherical cap geometry and 135σ for the cylindrical droplets. The bottom wall represents our substrate, which is unstructured and has infinite thickness [described by a potential given below[48] (Eq. 4)]. The top wall is implemented as a purely repulsive potential and its distance from the bottom wall (substrate) guarantees that the top wall does not interact with any of the simulated droplets. Additionally, the size of the simulation box in the z direction is large enough to guarantee that the two walls do not interact with each other due to the presence of the periodic boundary conditions in the z direction. For cylindrical droplets, the length L (Fig. 1d) is along the y direction. In this direction, periodic boundary conditions apply, while in the z and x directions the simulation box is large enough to guarantee that mirror images of the droplet do not interact with each other in these directions.

2.2 Statistical Associating Fluid Theory (SAFT-γ)

The SAFT-γ is a molecular-based equation of state (EoS) that analytically describes thermophysical data.[49] Computer simulations using the SAFT-γ Mie force-field have successfully elucidated the superspreading mechanism of surfactant-laden droplets on hydrophobic substrates.[7,50–52] Due to the close match between the theory and the underlying Hamiltonian of a system, the EoS offers an accurate fit for force-field parameters, which can be optimized to reproduce the macroscopically observed thermophysical properties and describe faithfully fluid–fluid and fluid–solid interactions.[39,40,50,53]

The SAFT approach involves the derivation of robust and transferable potentials of effective beads, which represent either a molecule, or a chemical moiety; the parameters can all be traced to macroscopic properties of the original segments of pure components.[50] These beads can be combined to describe heterogeneous chain fluids.[54] In our study, a bead denoted as 'W' represents two water molecules[49] (H_2O). Effective beads 'M' represent a chemical group $(CH_3)_3{-}Si{-}O_{\frac{1}{2}}$, and an effective bead 'D' corresponds to the group $O_{\frac{1}{2}}{-}(CH_3)_2{-}Si{-}O_{\frac{1}{2}}$. 'EO' effective beads represent $-CH_2{-}O{-}CH_2-$ (ether) chemical groups, while we make no distinction between terminal methyl groups and the CH_2 groups.[40] The masses of W, M, D, and EO effective beads are summarised in Table 1.

The non-bonded interactions between effective beads are described by the Mie potential, which is given by

$$U(r_{ij}) = C\varepsilon_{ij}\left[\left(\frac{\sigma_{ij}}{r_{ij}}\right)^{\lambda_{ij}^r} - \left(\frac{\sigma_{ij}}{r_{ij}}\right)^{\lambda_{ij}^a}\right] \tag{1}$$

where,

$$C = \left(\frac{\lambda_{ij}^r}{\lambda_{ij}^r - \lambda_{ij}^a}\right)\left(\frac{\lambda_{ij}^r}{\lambda_{ij}^a}\right)^{\left(\frac{\lambda_{ij}^a}{\lambda_{ij}^r - \lambda_{ij}^a}\right)}.$$

The indices i and j indicate the bead type (e.g., W, M, etc.). Thus, σ_{ij}, ε_{ij}, λ_{ij}^r, and λ_{ij}^a are parameters of the Mie potential, while r_{ij} is the distance between any two beads. The values of Mie potential parameters for different pairs of beads are summarised in Table 2 of the Appendix; the potential cutoff is 4.5834σ. In addition, we also have $\lambda_{ij}^a = 6$.

Surfactant molecules are built by binding effective beads with a harmonic potential:

$$V(r_{ij}) = 0.5k(r_{ij} - \sigma_{ij})^2, \tag{2}$$

where the values of σ_{ij} are given in Table 2, and $k = 295.33\varepsilon/\sigma^2$. Additionally, any three consecutive beads in each surfactant molecule of type EO interact via a harmonic angle potential

$$V_\theta(\theta_{ijk}) = 0.5k_\theta(\theta_{ijk} - \theta_0)^2, \tag{3}$$

where θ_{ijk} is the angle defined by three consecutive beads along the surfactant chain, $k_\theta = 4.32\varepsilon/rad^2$ is a constant, and $\theta_0 = 2.75rad$ is the equilibrium angle of the harmonic potential.

The fluid–substrate interactions were realised by an unbiased integration of the solid potential considering wall composed of spherical Mie beads.[48] The form of the potential reads

$$U_{sub}(D) = 2\pi\rho C\varepsilon_{ij}\sigma_{ij}^3\left[A\left(\frac{\sigma_{ij}}{D}\right)^{\lambda_{ij}^r-3} - B\left(\frac{\sigma_{ij}}{D}\right)^{\lambda_{ij}^a-3}\right], \tag{4}$$

Soft Matter Accepted Manuscript

This journal is © The Royal Society of Chemistry [year]

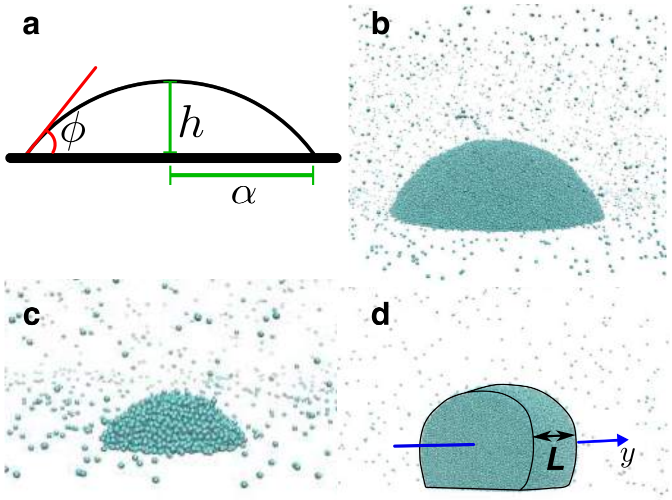

Fig. 1 (a) A cross-section of a spherical cap or cylindrical droplet, where the macroscopic contact angle ϕ, the height h and the radius α are indicated. Different snapshots of aqueous spherical cap (b,c) droplets on a hydrophilic substrate and a cylindrical droplet on a hydrophobic substrate ($\phi > \pi/2$) (d) are displayed. The length L is indicated for cylindrical droplets (d). The simulation snapshots are not scaled in the figures according to their size for the sake of clarity. For example, in case (c) the droplet is zoomed in considerably compared to cases (b) and (d) in order to highlight the structure of the LV interface and the CL. The average size $\langle N \rangle$ of each droplet is approximately: 2×10^5 (b), 4×10^3 (c), and 8×10^4 (d) beads. In case (d) periodic boundary conditions are applied in the y direction.

where $A = 1/(\lambda_{ij}^r - 2)(\lambda_{ij}^r - 3)$ and $B = 1/(\lambda_{ij}^a - 2)(\lambda_{ij}^a - 3)$. C, σ_{ij},ε_{ij}, λ_{ij}^r, and λ_{ij}^a have been defined in Eq. 1, ρ is the number density, which typically for a paraffinic substrate is $\rho \approx 1\sigma^{-3}$. D is the vertical distance between beads and the substrate. The cut-off of the fluid–substrate interaction is the same as the cut-off used for the fluid–fluid interactions. The substrate–water (SW) interaction is tuned to provide a contact angle of approximately 60° by setting the value of $\varepsilon_{\mathrm{SW}} = 1.4\varepsilon$ (cf., Fig. 2), from which one can obtain the substrate interaction parameter $\varepsilon_{\mathrm{SS}}$, while $\sigma_{\mathrm{SS}} = \sigma$. All other fluid–solid interactions arise from the use of common combination rules,[54] $\varepsilon_{ij} = (\sigma_{ii} + \sigma_{jj}/2)$, $\lambda_{ij}^r - 3 = \sqrt{(\lambda_{ii}^r - 3)(\lambda_{jj}^r - 3)}$, and $\varepsilon_{ij} = (1 - k_{ij})\sqrt{\sigma_{ii}^3 \sigma_{jj}^3 \varepsilon_{ii} \varepsilon_{jj}}/\sigma_{ij}^3$.

2.3 Aqueous droplets and estimation of contact angles

We assume that droplets have the same shape independently of their size since their shape is a result of free energy minimisation. This similarity in average equilibrium shape is expressed by the ratio $\lambda = h/\alpha$ (Fig. 1a), where h is the vertical distance between the droplet apex and the solid-liquid (SL) interface, and α is the radius of the SL interface.

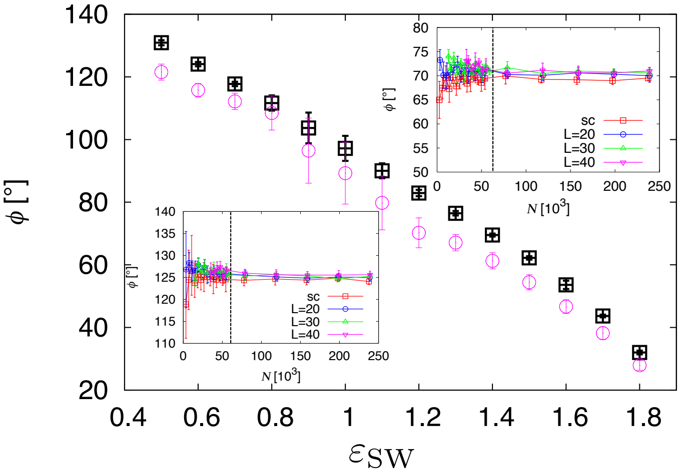

Fig. 2 Dependence of the contact angle on the substrate interaction $\varepsilon_{\mathrm{SW}}$ for a spherical cap droplet containing approximately on average 24×10^4 beads. Results have been obtained by applying Eq. 5 (squares) and a standard linear fitting method at the contact line (circles). Insets illustrate the dependence of the contact angle ϕ based on Eq. 5 as a function of the average number of beads in the droplet $\langle N \rangle$ for a hydrophobic substrate (bottom left) and a hydrophilic substrate (top right) for spherical cap droplets (sc) and cylindrical droplets with $L = 20$,30, and 40 σ. The vertical line indicates an approximate limit over which ϕ does not depend on the average number of beads $\langle N \rangle$. Lines are a guide for the eye.

The contact angle ϕ is given[56] by

$$\phi = \arcsin(1/\mu), \tag{5}$$

for hydrophilic substrates ($\phi < \pi/2$) for both cylindrical and spherical cap droplets, where $\mu = (1 + \lambda^2)/(2\lambda)$. For hydrophobic substrates, the contact angle will be $\phi' = \pi - \phi$. Hence, it suffices to measure the average droplet height $\langle h \rangle$ and the average radius $\langle \alpha \rangle$ in order to determine the average value of the contact angle $\phi = \langle \phi \rangle$. This is equivalent to the macroscopic contact angle of water (CAW) accessible to continuum theory or experiment.

In Fig. 2, we illustrate the dependence of the CAW ϕ on the interaction between water molecules and the solid substrate and compare the above method of measuring the contact angle ϕ to another using a linear fit applied on the liquid–vapour interface close to the contact line (CL). For the linear fit, the (liquid–vapour) LV interface is determined by identifying the most exterior beads belonging to the droplet. For this we use the Stillinger criterion[57] taking any pair of beads at a distance smaller than $1.5\sigma_{ij}$ to be part of the drop[7,58].

The calculation of the contact angle through the ratio λ overcomes the problems of fitting methods providing an accurate estimate of the CAW versus the substrate interaction $\varepsilon_{\mathrm{SW}}$, which in turn enables the evaluation of the parameter $\varepsilon_{\mathrm{SS}}$ of the

Soft Matter Accepted Manuscript

Soft Matter Accepted Manuscript

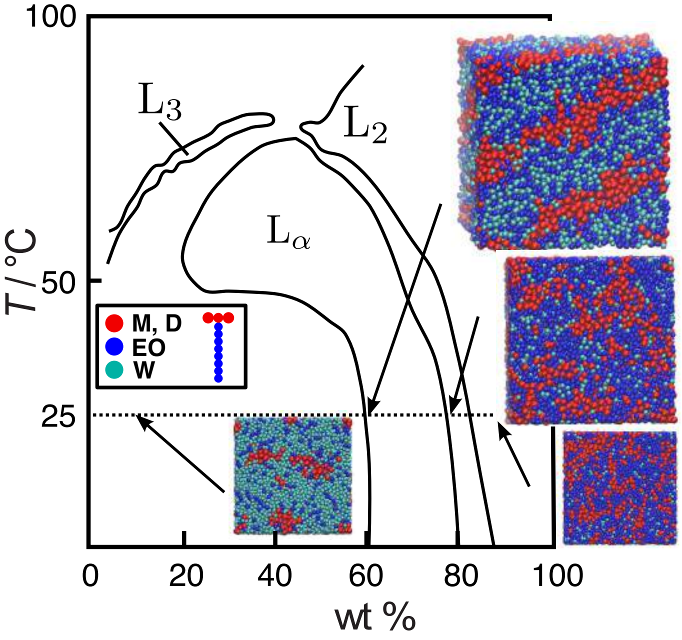

Fig. 3 Experimental phase diagram (Temperature vs. weight percent concentration [wt%]) for Silwet-L77. The experimental phase diagram has been adapted from Ref.[55]. Characteristic snapshots from our computer simulations based on the SAFT force field are also presented showing the characteristic fluid lamellar phase (L_α) in agreement with experiment. Colours indicate the type of beads as defined in the main text highlighting the distinction between surfactant hydrophobic beads (M, D), surfactant hydrophilic beads (EO), and water molecules (W). The T-shaped cartoon indicates the structure of the surfactant consisting of M-D-M beads (hydrophobic part) and eight EO (hydrophilic) beads, where the size of the beads is scaled according to their sizes (σ_{ii}) given in Table 2. Lines in the phase diagram do not indicate sharp phase boundaries as discussed in Ref.[55], in agreement with our simulations.

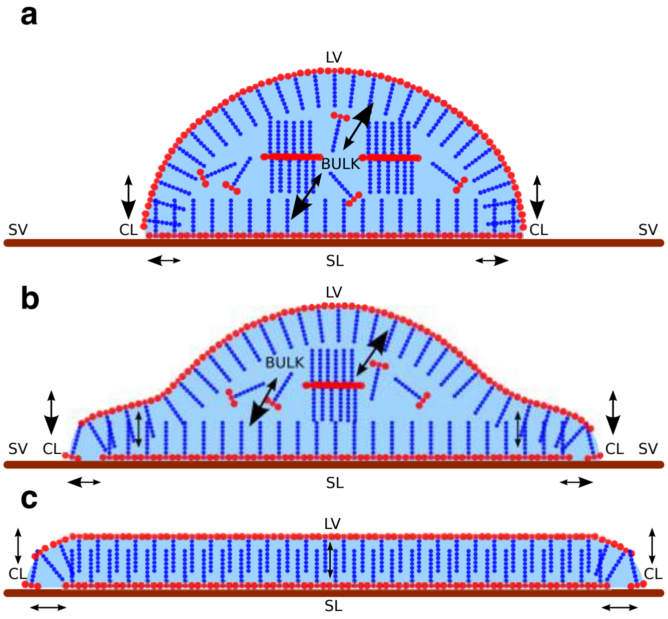

Fig. 4 Schematic illustration of a droplet cross-section and the leading adsorption processes taking place during superspreading, initially (a), at an intermediate stage (b) and at the final equilibrium state (c). Each dynamic adsorption process is indicated by a different arrow, where the arrow end of larger size indicates the dominant direction of mass transport, while the overall size of the arrows typifies the absolute magnitude of this adsorption process. Namely, the main adsorption processes of the superspreading mechanism are the hopping of surfactant from the LV to the SL interface through the contact line (CL), and the replenishment of surfactant at the interfaces (SL and LV) with surfactant coming from the bulk. The final stage is a bilayer (thin film), where surfactant molecules at liquid–vapour (LV) and solid–liquid (SL) interfaces are in dynamic equilibrium. Figure adapted from Ref.[7].

substrate. The results of Fig. 2 indicate a linear dependence with the substrate interaction which diverges slightly only at small contact angles. This is expected, since in this limit the droplet height becomes comparable to the potential cut-off. Moreover, statistical errors are significantly lower when Eq. 5 is applied versus those from the standard fitting method.

Fig. 2 illustrates also results for a spherical cap aqueous droplet containing around 24×10^4 beads, for which the contact angle ϕ does not depend on the droplet size. As presented in the insets of Fig. 2, droplets containing more than approximately 6×10^4 beads have reached the macroscopic limit of the contact angle, and, hence, we expect that the results for ϕ presented in the main panel of Fig. 2 for droplets containing 24×10^4 beads to be robust. The latter conclusion is valid irrespective of the substrate hydrophobicity (insets, Fig. 2), which is tuned through the interaction parameter $\varepsilon_{\mathrm{SW}}$. For droplets containing less than approximately 6×10^4 beads, the contact angle depends on the size of the droplet, and statistical error bars are larger indicating also larger fluctuations in the dimensions of the droplets. Standard scaling analysis suggests that this limit is closer to 7×10^4 beads,[59] but an exact determination of this limit has not been possible, and presumably is also model-dependent. Furthermore, we have compared these results with those based on a fitting method of estimating the CAW ϕ, and we found strong dependence of ϕ on the size of the droplet, in agreement with previous simulation results.[60] Moreover, the line tension[61] does not seem to play a significant role in the behaviour of large droplets. For small droplets, i.e., below 6×10^4 beads it is possible that the role of the line tension in determining ϕ may no longer be negligible.

In the following, we express properties of droplets as a function of droplet size through the ratio λ and the droplet radius α for aqueous droplets on hydrophilic substrates. For cylin-

This journal is © The Royal Society of Chemistry [year]

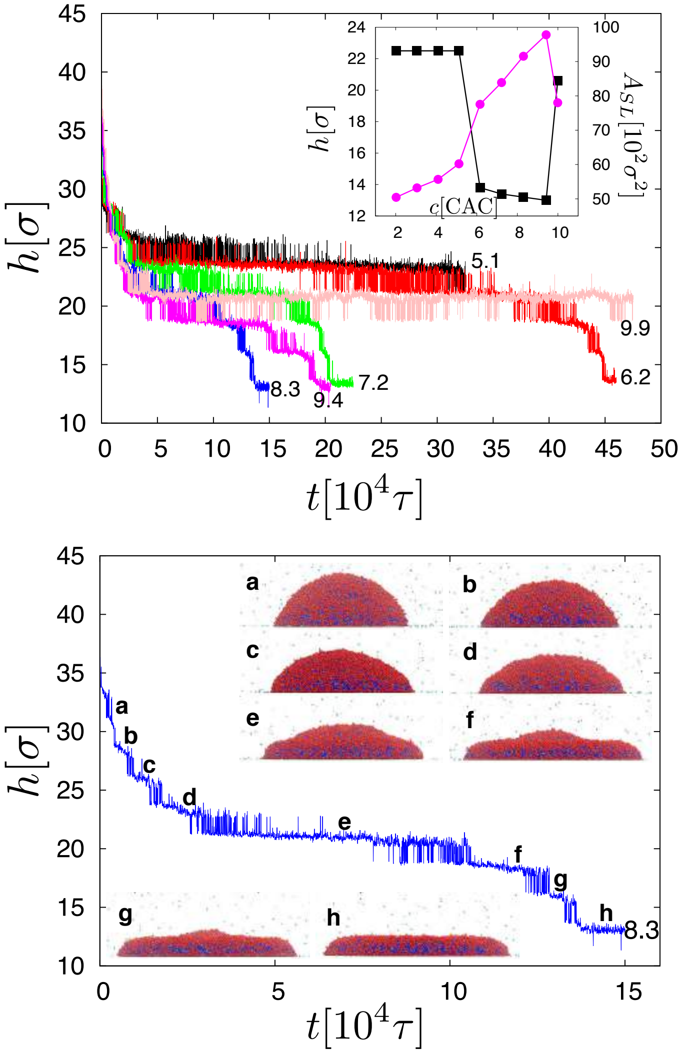

Fig. 5 Top panel: Height of the droplet as defined in the main text as a function of time for different concentrations as indicated. Inset displays the height (squares) and the final SL droplet area (circles) as a function of surfactant concentration. Lines are a guide for the eye. In the bottom panel, we chose the case of $c = 8.3$CAC, for which the fastest spreading occurs, in order to display simulation snapshots at different stages of the spreading process. Red colour corresponds to the hydrophobic moieties of Silwet-L77, blue to the hydrophilic groups, and cyan for water, the same as in Figs. 3 and 4. The scale of each snapshot is the same.

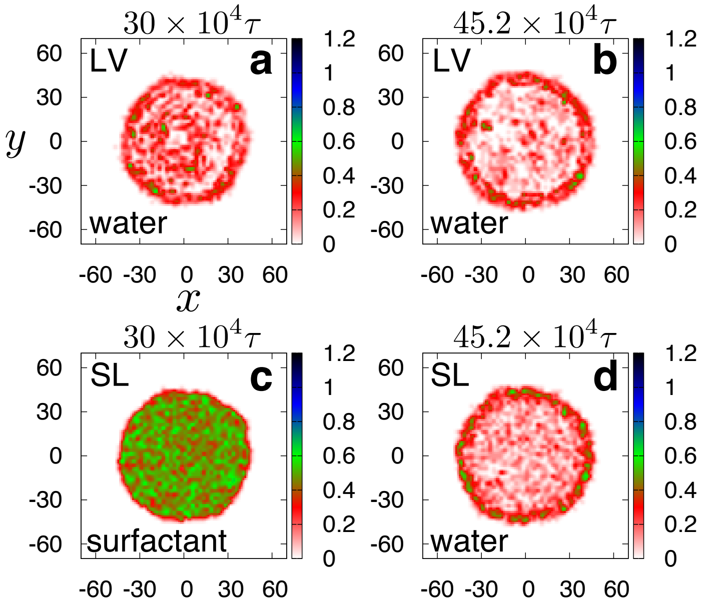

Fig. 6 Density of water or surfactant as indicated at the CWC (6.2CAC) seen from above (along the z direction) as a function of coordinates x and y. $0,0$ corresponds to the centre of the droplet. Density profiles have been calculated at the times shown for each column, i.e., an intermediate time corresponding to states such as that of Fig. 4b ($30\times10^4\tau$) and a later time corresponding to states described schematically by Fig. 4c ($45.2\times10^4\tau$). Panels (a) and (b) illustrate the density of water molecules on the LV interface, panel (c) the density of surfactant molecules on the SL interface, and panel (d) the density profile of water beads on the SL interface.

drical droplets (Fig. 1c,d), $A^c_{LV} = 2\alpha\mu L\phi$, $A^c_{SL} = 2aL$, and $V^c = \alpha^2\nu L$, where ν depends only on the ratio λ, i.e., $\nu = \mu^2\phi - \mu\sqrt{1-(1/\mu)^2}$. μ and ϕ have been defined previously and L is the length of the cylindrical droplet (Fig. 1c,d). For droplets of spherical cap shape (Fig. 1b, c), $A^{sc}_{LV} = \alpha^2\pi(1+\lambda^2)$, $A^{sc}_{SL} = \alpha^2\pi$, and $V^{sc} = \alpha^3\pi\lambda(3+\lambda^2)/6$. These relations[62] clearly indicate that the computational cost of simulating cylindrical droplets over spherical droplets scales as L/α. Indeed, the values of contact angle ϕ for droplets with more than 6×10^4 beads are the same within the statistical error for cylindrical droplets of different L and spherical cap droplets justifying the use of cylindrical droplets in computer simulations if the ratio L/α is chosen correctly. Notwithstanding, for more complex scenarios, suach as surfactant-laden aqueous systems, it is unproven that the results from cylindrical droplets are equivalent to that of spherical droplets; hence, the latter will be used herein.

Soft Matter Accepted Manuscript

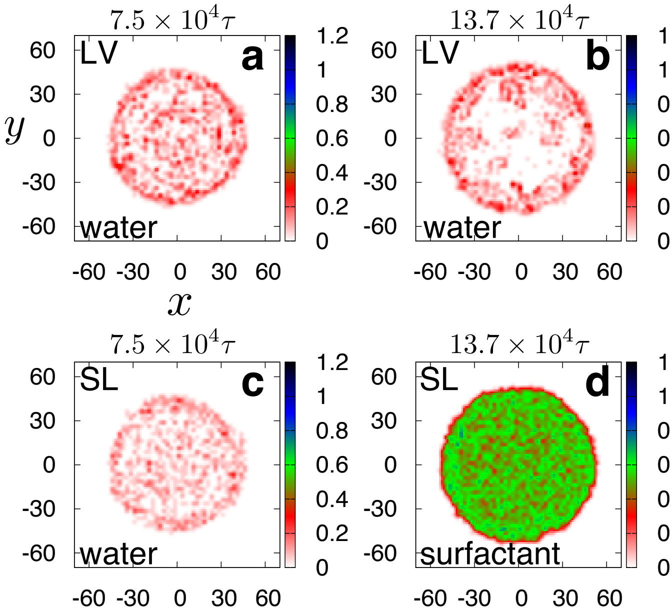

Fig. 7 Density of water or surfactant as indicated at 8.3CAC seen from above (along the z direction) as a function of coordinates x and y. For this surfactant concentration the fastest spreading takes place. $0,0$ corresponds to the centre of the droplet. Density profiles have been calculated at the times shown for each column, i.e., an intermediate time corresponding to states such as that of Fig. 4b ($7.5 \times 10^4 \tau$) and a later time corresponding to states described schematically by Fig. 4c ($13.7 \times 10^4 \tau$). Panels (a) and (b) illustrate the density of water molecules on the LV interface, panel (c) the destiny of water molecules on the SL interface, and panel (d) the density profile of surfactant beads on the SL interface.

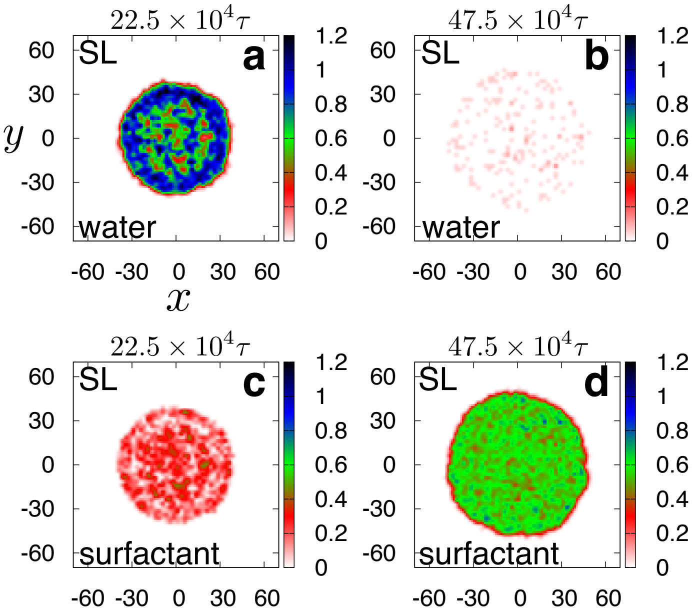

Fig. 8 Density profiles for a droplet having 2CAC surfactant concentration at time $22.5 \times 10^4 \tau$ and a droplet having 10CAC surfactant concentration at time $47.5 \times 10^4 \tau$. Panels (a, b) illustrate the density of water molecules on the SL interface, and (c, d) the density of surfactant beads on the SL interface. The shape of the droplet in both cases (low and large concentrations) resembles that of Fig. 4a.

3 Results for Surfactant-laden aqueous systems

3.1 Bulk phase Behaviour of Silwet-L77 surfactant

Simulations based on the SAFT force-field are able to describe the fluid–fluid interactions of surfactant aqueous solutions in the bulk. This is powerfully evidenced by the qualitative comparison of experimental phase behaviour[55] to the behaviour observed in our computer simulations (Fig. 3). In the case of Silwet-L77 surfactant, our model obtains the experimentally observed characteristic fluid lamellar (L_α) structure.[55] Moreover, our simulations provide an overall qualitative description of the behaviour of this system. The ability of the SAFT force-field to reliably represent the fluid–fluid interactions between moieties and water molecules is indispensable for modelling the superspreading mechanism.

Similarly, the phase behaviour observed experimentally for C10E8 surfactant[63] (not shown here), which is a nonsuperspreading surfactant, agrees very well with our computer simulations based on the SAFT force-field, as well as in many other cases of nonanionic surfactants in aqueous solutions.[40] For C10E8 surfactants, we have obtained in our simulations the characteristic hexagonal phase (cylinders) for high surfactant concentrations in agreement with experimental observation.[63] In addition, we have observed the formation of micellar-type structures at low to intermediate concentrations, while combinations of hexagonal and lamellar structures appear at higher surfactant concentration. Various phase diagrams based on the SAFT force field for other poly-alkyl-ether surfactants and details on the parameterization of these surfactant moieties validating the SAFT force-field have been recently provided by Lobanova in her thesis.[40]

3.2 Superspreading of droplets

Previously, Theodorakis *et al.*[7] found that the first element of superspreading mechanism is the adsorption of surfactant onto the substrate through the CL (see Fig. 4) confirming the conclusions by Karapetsas *et al.*[64] Crucially, this adsorption process must be followed by the replenishment of the LV and SL interfaces with surfactants from the interior of the droplet.[7,64] At some point, a bilayer forms at the CL and a rapid spreading process follows, as observed in experiments.[65,66] Also, we have reported that the T-shaped geometry favours the spread-

Soft Matter Accepted Manuscript

This journal is © The Royal Society of Chemistry [year]

ing process, which, for superspreading surfactants, exhibits a maximum with the increase of surfactant concentration.[9] Although the basic machanism is understood, it is now known that a plethora of different factors can suppress or aid superspreading behaviour.

A key surrogate quantity to monitor superspreading is the droplet height, h. For hydrophobic substrates, the hydrophobic moiety of the surfactant attaches to the substrate increasing the size of the droplet in the planar directions. As a result, the height h of the droplet decreases due to mass conservation. At this point, we observe that the droplet oscillates between two states, until the replenishment of the interfaces has been completed. Moreover, we observe that the time required for replenishment of the interfaces with surfactant varies, while we can discern a prolonged intermediate state during the spreading (Fig. 5a). Following interface replenishment, the dragging process at the CL is facilitated due to the low surface tensions of the interfaces, resulting in the further increase of the droplet area. The whole process continues, until the occurrence of the thin film formation and the establishment of dynamic equilibrium (Fig. 4).

We have also observed the spreading to be faster, and the height to reduce more rapidly, as the surfactant concentration increases, reaching a maximal value for certain concentration (Fig. 5a).[7] For very high concentrations, we observe that the surfactant reduces its superspreading ability (Fig. 5a), in agreement with experimental observations.[9]

The final values of droplet height, which are displayed in the inset of Fig. 5a indicate the same value of height within the statistical error for small surfactant concentrations, where the effect of surfactant is small. At a certain surfactant concentration, which is known as the Critical Wetting Concentration (CWC) we observe that the droplet height reduces dramatically (cf. Fig. 4c) to very similar values. Further increase in surfactant concentration results in an abrupt increase of the droplet height, i.e., a deterioration of the spreading rate. On the other hand, the final area of the SL interface A_{SL} displays a smoother variation with surfactant concentration (inset of Fig. 5a). The latter may provide a hint that the height h of the droplet is related to the replenishment element of the superspreading mechanism, whereas the area is a property closer linked to the adsorption of surfactant from the LV interface onto the substrate through the CL. Therefore, variations of the height h could provide an estimate of the time that surfactant molecules need to replenish the interfaces. Additionally, this time appears to be strongly correlated with the different stages of superspreading and the geometry of the LV interface (Fig. 5b). This is evidenced by the appearance of the bilayer formation (cf. stage e of the droplet in Fig. 5b), where a significant change in the droplet shape begins to takes place, characterised by the onset of thin film formation. The above discussion on the superspreading of surfactant-laden droplets share some similarities regarding the structure of the droplets with the voltage-induced superspreading of liquids on moderately hydrophobic substates, which can be captured by high speed video cameras.[67]

The rapid rate of reduction in the droplet height in the latter stages of spreading (Fig. 5) is explained by the small size of the droplet, which amounts only to a few tens of nanometres (e.g., from a droplet diameter of 30nm for the case of Fig. 4a to 60nm for the case of Fig. 4b[7]). This is also manifested by results on the density profiles (Figs. 6, 7 and supplementary material), which reveal the size and the shape of the droplet at a particular time corresponding to an intermediate state (cf. Fig. 4b) and a later time corresponding to the final equilibrium configuration of Fig. 4c or similar to that of Fig. 5f.

The water and surfactant molecules are homogenously distributed across the bulk of the droplet at any time during the spreading process, and the overall density of the droplets also remains constant, as shown in Fig. 6 (and in the supplementary information) for a droplet at the CWC. However, by monitoring the surfactant at the LV interfaces (the dimension of each box element containing the interface beads is $2\sigma_{\mathrm{MM}}$), we observe that the amount of water molecules at the interfaces decreases as water is 'sandwiched' between the LV and SL interfaces. The area close to the CL has a significant amount of water, however, as it is exposed to the CL, where surfactant adsorbs directly from the LV interface onto the substrate. The same is true for the local density at the SL interface: water molecules are exposed to the vapour because of the formation of the bilayer, the adsorption from the LV onto the substrate through the CL, and the drag of water molecules from surfactant molecules at the CL area.

We observe no discernible pattern for the local density of surfactant molecules at any of the SL or LV interfaces, indicating that the geometry of the droplet during the spreading process does not affect the distribution of surfactant on these interfaces. This is observed at all times during the spreading process, and not only at the times indicated in Fig. 6. We only observe a small decrease in the density of surfactant at the LV interface, as the droplet assumes a thin film shape (Fig. 6), which becomes more apparent for droplets with higher surfactant concentration (Fig. 7). For the latter case, similar effects are observed, but the patterns of the local density are more apparent in the case of the surfactant density profiles, clearly, due to the high concentration of surfactant.

The density profiles for droplets at low (2CAC) and high (10CAC) concentration (Fig. 8 and supplementary info), where no superspreading is observed, differ considerably with the superspreading densities of Figs. 6 and 7 (see also supplementary information); here, CAC is the critical aggregation concentration. For low concentration, the LV interface has a higher density of water compared to the superspreading cases, despite being at a concentration two times higher than

Soft Matter Accepted Manuscript

the CAC. For high concentrations, the density profile of water at the LV interface shows a more homogeneous structure than the ring pattern (higher density close to the LV interface) apparent in the superspreading regime (see Fig. 8 and supplementary information). Moreover, the density of surfactant at the LV interface for low concentration (but still above the CAC), is lower than the superspreading cases. For low concentrations, the SL interface is dominated by water molecules.

We have also monitored the time spent by each surfactant molecule at various regions of the droplets, i.e., the SL and LV interfaces, the CL, and the bulk. During the spreading of the droplets and for the superspreading cases, we have found that a significant amount of surfactant visited the SL and LV interfaces; the probability of surfactants being at the LV interface is higher, because the latter can accomodate a larger number of surfactants than the SL interface at a lower energy. Only a small fraction of surfactants spend up to 40% of their time at the CL during the spreading process. Finally, there are surfactants which never become part of the bulk of the droplet, which is related to the small size of the simulated droplets.

4 Summary and outlook

In this work, we have discussed the modelling of surfactant-laden droplets in the context of superspreading. We have presented a simple method for obtaining contact angles reliably at the macroscopic scale and identified the limit where the contact angle becomes independent of the droplet size for this model, in agreement with previous simulations studies by Santiso *et al.*.[60] We have also provided characteristic examples that validate the use of SAFT force fields in computer simulations as a coarse-graining tool that reproduces faithfully macroscopic properties. Moreover, we have discussed details of properties pertaining to the superspreading phenomenon, providing details of the structural properties of the droplets during superspreading. This work elucidates the mechanism of superspreading, extending the work of Theodorakis *et al.*[6] and providing a basis for *in silico* design of surfactants for coating flow applications.

Acknowledgements

We gratefully acknowledge funding for our work provided by the Engineering and Physical Sciences Research Council (EPSRC), U.K., through grants EP/J010502, EP/I018212, EP/J014958, and EP/L020564. We express our gratitude to N. Kovalchuk and V. Starov from the University of Loughborough for fruitful discussions. We also thank Sadia Rahman for providing the SAFT parameters for the siloxane groups. The authors acknowledge support from the Thomas Young Centre under grant TYC-101. Our simulations were carried out at the GPGPU server in the Mathematics Department at Imperial College London.

Table 1 The masses of M, D, W and EO effective beads in reduced mass units.

	W	M	D	EO
Mass $[m]$	0.8179	1.8588	1.6833	1.0000

Table 2 The parameters of the Mie potential for the interactions between beads. $\lambda^a_{ij} = 6$ in all cases.

i-j	$\sigma_{ij}[\sigma]$	$\varepsilon_{ij}[\varepsilon/k_B]$	λ^r_{ij}
W-W	0.8584	0.8129	8.00
W-M	1.0491	0.8132	13.72
W-D	0.9643	0.6311	10.38
W-EO	0.8946	0.9756	11.94
M-M	1.2398	0.8998	26.00
M-D	1.1550	0.7114	18.83
M-EO	1.0853	0.8262	22.18
D-D	1.0702	0.5081	13.90
D-EO	1.0004	0.6355	16.21
EO-EO	0.9307	0.8067	19.00

5 Appendix

Here, we provide a summary of the force field parameters. Reduced and real units are related as follows: $\sigma = 0.43635$nm, $\varepsilon/k_B = 492$K, $m = 44.0521$amu, and the $\tau = 1.4062$ps.

References

1 P.-G. deGennes, F. Brochard-Wyart and D. Quéré, *Capillarity and Wetting Phenomena: Drops, Bubbles, Pearls, Waves*, Springer, 2004.
2 D. Bonn, J. Eggers, J. Indekeu, J. Meunier and E. Rolley, *Reviews of Modern Physics*, 2009, **81**, 739–805.
3 R. V. Craster and O. K. Matar, *Reviews of Modern Physics*, 2009, **81**, 1131–1198.
4 O. K. Matar and R. V. Craster, *Soft Matter*, 2009, **5**, 3801–3809.
5 M. J. Rosen and J. T. Kunjappu, *Surfactants and Interfacial Phenomena*, John Wiley & Sons, New Jersey, 4th edn, 2012, p. 600.
6 P. E. Theodorakis, E. A. Müller, R. V. Craster and O. K. Matar, *Curr. Opin. Colloid Interface Sci.*, 2014, **19**, 283–289.
7 P. E. Theodorakis, E. A. Müller, R. V. Craster and O. K. Matar, *Langmuir*, 2015, **31**, 2304–2309.
8 E. G. Schwarz and W. G. Reid, *Ind. Eng. Chem.*, 1964, **56**, 26–35.
9 R. M. Hill, *Curr. Opin. Colloid Interface Sci.*, 1998, **3**, 247–254.
10 A. Nikolov and D. Wasan, *Eur. Phys. J.: Spec. Top.*, 2011, **197**, 325–341.
11 J. Venzmer, *Curr. Opin. Colloid Interface Sci.*, 2011, **16**, 335–343.
12 K. P. Ananthapadmanabhan, E. D. Goddard and P. A. Chandar, *Colloids Surf.*, 1990, **44**, 281–297.
13 S. Rafaï, S. Dipak, V. Bergeron, J. Meunier and D. Bonn, *Langmuir*, 2002, **18**, 10486–10488.
14 J. Hautman and K. M. L., *Phys. Rev. Lett.*, 1991, **67**, 1763–1766.

Soft Matter Accepted Manuscript

This journal is © The Royal Society of Chemistry [year]

15 W. Mar and K. M. L., *J. Phys.: Condens. Matter*, 1994, **6**, A381–A388.
16 C. F. Fan and C. T., *J. Chem. Phys.*, 1995, **103**, 9053–9061.
17 J. M. D. Lane, M. Chandross, C. D. Lorenz, M. J. Stevens and G. S. Grest, *Langmuir*, 2008, **24**, 5734–5739.
18 G. Saville, *J. Chem. Soc., Faraday Trans. 2*, 1977, **73**, 1122–1132.
19 J. Sikkenk, J. Indekeu, J. van Leeuwen, E. Vossnack and A. Bakker, *J. Stat. Phys.*, 1988, **52**, 23–44.
20 M. Nijmeijer, C. Bruin, A. Bakker and J. V. Leeuwen, *Physica A: Statistical Mechanics and its Applications*, 1989, **160**, 166 – 180.
21 M. J. P. Nijmeijer, C. Bruin, A. F. Bakker and J. M. J. van Leeuwen, *Phys. Rev. A*, 1990, **42**, 6052–6059.
22 J. A. Nieminen and T. Ala-Nissila, *EPL (Europhysics Letters)*, 1994, **25**, 593.
23 J. A. Nieminen and T. Ala-Nissila, *Phys. Rev. E*, 1994, **49**, 4228–4236.
24 M. J. de Ruijter, T. D. Blake and J. De Coninck, *Langmuir*, 1999, **15**, 7836–7847.
25 T. Blake, A. Clarke, J. D. Coninck, M. de Ruijter and M. Voué, *Colloids and Surfaces A: Physicochemical and Engineering Aspects*, 1999, **149**, 123 – 130.
26 T. Blake, C. Decamps, J. D. Coninck, M. de Ruijter and M. Voué", *Colloids and Surfaces A: Physicochemical and Engineering Aspects*, 1999, **154**, 5 – 11.
27 M. Voué, S. Semal and J. De Coninck, *Langmuir*, 1999, **15**, 7855–7862.
28 M. Voué, S. Rovillard, J. De Coninck, M. P. Valignat and A. M. Cazabat, *Langmuir*, 2000, **16**, 1428–1435.
29 M. Voué and J. D. Coninck, *Acta Mater.*, 2000, **48**, 4405 – 4417.
30 J. D. Coninck, M. J. de Ruijter and M. Voué, *Current Opin. Colloid Interface Sci.*, 2001, **6**, 49 – 53.
31 M. Lundgren, N. L. Allan, T. Cosgrove and N. George, *Langmuir*, 2002, **18**, 10462–10466.
32 M. Lundgren, N. L. Allan, T. Cosgrove and N. George, *Langmuir*, 2003, **19**, 7127–7129.
33 D. R. Heine, G. S. Grest and E. B. Webb, *Phys. Rev. E*, 2003, **68**, 061603.
34 T. Werder, J. H. Walther, R. L. Jaffe, T. Halicioglu and P. Koumoutsakos, *J. Phys. Chem.*, 2003, **107**, 1345–1352.
35 M. S. Tomassone, A. Couzis, C. M. Maldarelli, J. R. Banavar and J. Koplik, *J. Chem. Phys.*, 2001, **115**, 8634–8642.
36 M. S. Tomassone, A. Couzis, C. M. Maldarelli, J. R. Banavar and J. Koplik, *Langmuir*, 2001, **17**, 6037–6040.
37 W. Shinoda, R. DeVane and M. L. Klein, *Molecular Simulation*, 2007, **33**, 27–36.
38 W. Shinoda, R. DeVane and M. L. Klein, *Soft Matter*, 2008, **4**, 2454–2462.
39 C. Herdes, E. E. Santiso, C. James, J. Eastoe and E. A. Müller, *J. Colloid Interface Sci.*, 2015, **445**, 16–23.
40 O. Lobanova, *PhD thesis*, Imperial College London, 2014.
41 R. E. Isele-Holder and A. E. Ismail, *J. Phys. Chem. B*, 2014, **118**, 9284–9297.
42 Y. Shen, A. Couzis, J. Koplik, C. Maldarelli and M. S. Tomassone, *Langmuir*, 2005, **21**, 12160–12170.
43 H.-Y. Kim, Q. Yin and K. A. Fichthorn, *J. Chem. Phys.*, 2006, **125**, 174708.
44 J. D. Halverson, C. Maldarelli, A. Couzis and J. Koplik, *Chem. Eng. Sci.*, 2009, **64**, 4657–4667.
45 D. Sergi, G. Scocchi and A. Ortona, *J. Chem. Phys.*, 2012, **137**, 094904.
46 R. E. Isele-Holder, B. Berkels and A. E. Ismail, *Soft Matter*, 2015, **11**, 4527–4539.
47 J. A. Anderson, C. D. Lorenz and A. Travesset, *J. Comput. Phys.*, 2008, **227**, 5342–5359.
48 E. Forte, A. J. Haslam, G. Jackson and E. A. Müller, *Phys. Chem. Chem. Phys.*, 2014, **16**, 19165–19180.
49 O. Lobanova, C. Avendaño, T. Lafitte, E. A. Müller and G. Jackson, *Mol. Phys.*, 2015, **113**, 1228–1249.
50 E. A. Müller and G. Jackson, *Annu. Rev. Chem. Biomol. Eng.*, 2014, **5**, 405–427.
51 C. Avendaño, T. Lafitte, A. Galindo, C. S. Adjiman, G. Jackson and E. A. Müller, *J. Phys. Chem B*, 2011, **115**, 11154–11169.
52 C. Avendaño, T. Lafitte, A. Galindo, C. S. Adjiman, E. A. Müller and G. Jackson, *J. Phys. Chem B*, 2013, **117**, 2717–2733.
53 V. Papaioannou, T. Lafitte, C. Avendaño, C. S. Adjiman, G. Jackson, E. A. Müller and A. Galindo, *J. Chem. Phys.*, 2014, **140**, 054107.
54 T. Lafitte, A. Apostolakou, C. Avendaño, A. Galindo, C. S. Adjiman, E. A. Müller and G. Jackson, *J. Chem. Phys.*, 2013, **139**, 154504.
55 R. M. Hill, M. He, H. T. Davis and L. E. Scriven, *Langmuir*, 1994, **10**, 1724–1734.
56 F. Leroy and F. Müller-Plathe, *J. Chem. Phys.*, 2010, **133**, 044110.
57 F. H. Stillinger, *J. Chem. Phys.*, 1963, **38**, 1486.
58 P. E. Theodorakis, W. Paul and K. Binder, *J. Chem. Phys.*, 2010, **133**, 104901.
59 O. Melchert and A. K. Hartmann, *Phys. Rev. B*, 2009, **79**, 184402.
60 E. E. Santiso, C. Herdes and E. A. Müller, *Entropy*, 2013, **15**, 3734–3745.
61 J. H. Weijs, A. Marchand, B. Andreotti, D. Lohse and J. H. Snoeijer, *Phys. Fluids*, 2011, **23**, 022001.
62 J. W. Harris and H. Stocker, *Handbook of Mathematics and Computational Science*, Springer Verlag, New York, 1998.
63 Y. Nibu and T. Inoue, *J. Colloid Interface Sci.*, 1998, **205**, 305–315.
64 G. Karapetsas, R. V. Craster and O. K. Matar, *J. Fluid Mech.*, 2011, **670**, 5–37.
65 F. Tiberg and C.-M. Cazabat, *Europhys. Lett.*, 1994, **25**, 205–210.
66 E. Ruckenstein, *Colloids Surf., A*, 2012, **412**, 36–37.
67 G. McHale, C. V. Brown and N. Sampara, *Nature Comm.*, 2013, **4**, 1605.

Soft Matter Accepted Manuscript

Modelling the superspreading of surfactant-laden droplets with computer simulation

P.E. Theodorakis, E. A. Müller, R. V. Craster & O. K. Matar
Department of Chemical Engineering & Department of Mathematics, Imperial College London

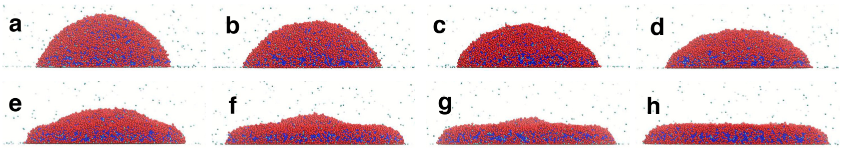

The key elements of superspreading mechanism are the adsorption of surfactant from the liquid-vapour interface onto the substrate through the contact-line and the replenishment of interface with surfactant from the bulk. These elements manifest themselves in various properties of the droplets. We provide an in-depth analysis of the superspreading phenomenon, details allowing for the modelling of this phenomenon, and a way to estimate accurately the macroscopic contact angle in aqueous droplets. Figure illustrates different states of the droplet during superspreading.

Soft Matter Accepted Manuscript